# Electrochemical Growth of ZnO Nanobelt-Like Structures at 0 °C: Synthesis, Characterization, and in-Situ Glucose Oxidase Embedment

Debabrata Pradhan,[†] Zhengding Su, Shrey Sindhwani, John F. Honek, and Kam Tong Leung*

Department of Chemistry, University of Waterloo, Waterloo, Ontario N2L 3G1, Canada

ABSTRACT: Single-crystalline ZnO nanobelt-like structures (NBS) of length, width, and thickness in the ranges of 5—10 μm, 50—400 nm, and 20—100 nm, respectively, are synthesized by a one-step, template-free electrochemical deposition technique at 0 °C. Scanning electron microscopy and transmission electron microscopy (TEM) reveal a unique morphology of the as-synthesized NBS, with an oval-shaped cross section. High-resolution TEM and selected area electron diffraction studies further confirm that individual NBS are single-crystalline, with a growth direction of $[10\bar{1}0]$, while the X-ray diffraction data indicate its characteristic wurtzite structure. The successful formation of ZnO NBS at 0 °C using this simple, aqueous-solution-based, bottom-up approach is further exploited to fabricate a bionanocomposite. In particular, incorporation of a biomolecule, i.e., glucose oxidase (GOx) into the ZnO NBS in situ during electrodeposition is found to be highly effective in enhancing the activity and stability. The resulting GOx-embedded ZnO NBS are found to exhibit not only a higher enzymatic activity but also remarkable stability when compared to GOx surface-immobilized ZnO NBS. The present direct biomolecular embedment approach promises a new strategy for incorporating other compatible biomolecules in situ at low temperature while preserving their bioactivity.
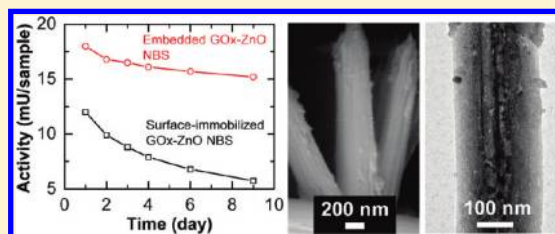
1. INTRODUCTION

ZnO is one of the transparent conducting oxide semiconductors with a high technological demand in the fields of optoelectronics, catalysis, rubber industry, and cosmetics. The last few years have witnessed the synthesis of a wide variety of ZnO nanostructures by both thermal evaporation[1−3] and wet-chemistry methods.[4−7] The use of high temperature (500—1000 °C) in these thermal evaporation techniques necessitates a larger energy consumption and more expensive, heat-tolerable substrates, such as silicon and sapphire, to deposit the ZnO nanomaterials. In contrast, wet-chemistry methods such as hydrothermal,[5,8] sol—gel,[9,10] chemical bath deposition,[11−13] and electrodeposition[6] require a far lower synthesis temperature (70—200 °C), allowing "greener" development of nanomaterials on low-cost glass[5,14] and flexible plastic substrates.[15−17] To date, several attempts have been made to synthesize ZnO and other inorganic semiconducting oxide materials at room temperature,[18−24] which also makes viable potential biological applications. As bacteria and viruses have been found to provide ordering of inorganic nanocrystals into novel architectures in nanomaterials,[25−28] an in situ, flexible synthetic procedure capable of producing nanostructured materials in bulk quantities at a low temperature without incapacitating these living organisms would be highly desirable in the development of biologically active nanocomposites. Recently, Rica et al. successfully used an enzyme urease as a catalytic template to grow crystalline ZnO nanoshells at room temperature.[18] There is high potential to incorporate other biomolecules to engineer the nanostructured materials in situ during the synthesis process, provided that the process can be conducted at a "bio-friendly" temperature (below room temperature) without significantly impeding on the desired yield.

Since the first report of quasi one-dimensional (1D) ZnO nanomaterials, i.e., nanobelt, synthesized by thermal evaporation of ZnO powders at 1400 °C onto an alumina substrate by Pan et al.,[29] ZnO nanobelts have been used in several applications.[30−32] These quasi 1D ZnO nanobelts have not only specific axial growth but also well-defined side facets, unlike the more common 1D nanomaterials (e.g., nanowires and nanotubes) that grow along an axial direction without any well-defined growth in the lateral direction.[33] There are only a few reports of producing ZnO nanobelts using the lower-temperature wet chemistry methods, where the synthesis has been successfully attempted from 200 °C down to room temperature.[21,34] As most biologically active materials and living organisms are more stable below room temperature,[35] the water freezing point would therefore represent the ultimate temperature to develop biologically active nanomaterials involving aqueous solution chemistry. By varying different electrodeposition parameters, we controlled the growth conditions to successfully produce quasi 1D ZnO nanobelt-like structures (NBS) at 0 °C on two different conducting substrates, a flexible $In_2O_3/Au/Ag$ coated polyethylene terephthalate (PET) and an indium—tin-oxide coated glass (ITO-glass) substrate, by using a one-step, template-free electrochemical deposition technique. To our best knowledge, such synthesis of ZnO nanostructures below room temperature has never been reported. To demonstrate the advantage of this low-temperature synthesis technique, we performed direct incorporation of an enzyme, i.e., glucose oxidase (GOx
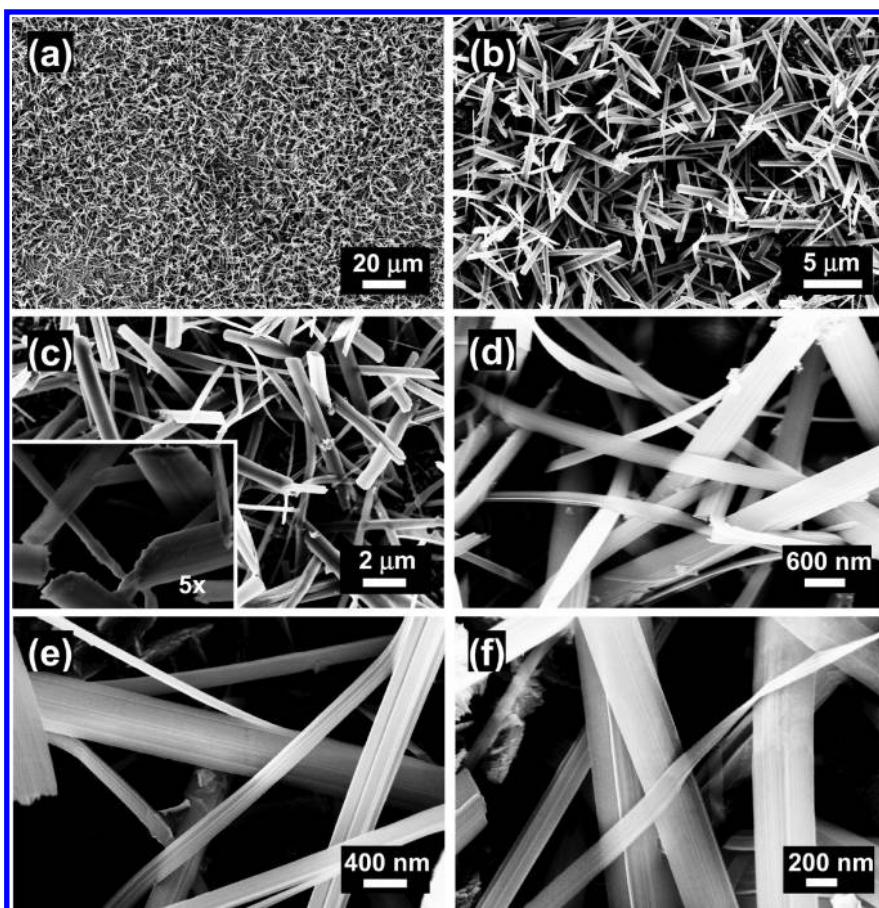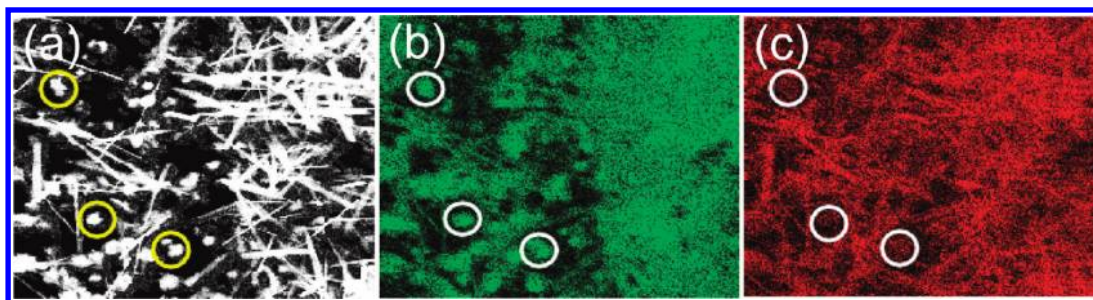
Figure 1. SEM images of ZnO nanobelt-like structures electrodeposited on a conducting PET substrate at 0 °C in 0.1 M $Zn(NO_3)_2 \cdot 6H_2O$ mixed with 0.1 M KCl electrolyte for 180 min.

(GOx), into ZnO NBS during material growth to produce a nanocomposite. In the past, biomolecules have generally been attached to the surface of the material by either physical (such as adsorption, entrapment, or encapsulation) or chemical (such as cross-linking, covalent bonding, or electrochemical polymerization) methods after the material is formed.[36] Despite several recent studies on biofunctionalization[37−39] and surface immobilization of biomolecules,[40−43] onto nanomaterials for applications in drug delivery,[37] tissue engineering,[42] and biosensors,[43] no study has been reported on embedding biomolecules directly into an inorganic host nanomaterial in situ during growth. This manner of direct incorporation is particularly challenging due to the requirements of not only the presence of an aqueous medium but also a low growth temperature, preferably below room temperature, to preserve the activity of biomolecules during the nanomaterial growth. The present approach of direct embedding of biomolecules into nanostructure during growth could provide the performance enhancement[44] and new possibilities in such applications as slow-release drug delivery and extended-use biosensors. GOx is known to be a widely used enzyme in studies on the surface immobilization of various nanomaterials for biosensor applications (particularly for monitoring blood sugar levels in diabetic patients).[40] The preparation of ZnO nanomaterials at 0 °C and direct incorporation of GOx into ZnO NBS during the low-temperature growth paves a new way of fabricating other bioactive nanocomposites appropriate for a wide range of applications.

2. MATERIALS AND METHODS

2.1. Synthesis of ZnO Nanobelt-Like Structures. A conventional three-electrode electrochemical glass cell placed in an ice bath was used for the ZnO NBS growth. A 10 mL solution of 0.1 M $Zn(NO_3)_2 \cdot 6H_2O$ mixed with 0.1 M KCl (both from Aldrich) was used as the electrolyte to produce NBS. To incorporate GOx into the NBS during growth, 5 mg of GOx (211 U/mg, Fluka) was added to the above electrolyte. Surface immobilization of ZnO NBS was carried out by dipping the NBS sample into the same phosphate buffer solution of GOx (with the same concentration) for 24 h at 4 °C. The working electrode was either an In_2O_3/Au/Ag-coated PET or an ITO-coated glass substrate, with a sheet resistance ≤10 Ω (Delta Technologies Limited, Minnesota). Cathodic electrodeposition was carried out at an applied potential of −1.4 V with respect to the Ag/AgCl reference electrode, with a Pt wire serving as the counter electrode. After the deposition, the samples were washed thoroughly several times with Milli-Q water and dried in a nitrogen-filled box overnight before characterization. All GOx-incorporated samples were stored at 4 °C.

2.2. Characterization. The surface morphologies and composition of the electrodeposits were examined by using a LEO FESEM 1530 field-emission scanning electron microscope (SEM), equipped with an EDAX Pegasus 1200 energy-dispersive X-ray analysis system (EDX). The crystal structure of the nanodeposits was characterized by X-ray diffraction (XRD) using

Figure 2. (a) SEM image and elemental EDX maps of (b) Zn K_α and (c) O K_α for nanobelt-like structures electrodeposited on a conducting PET substrate at 0 °C for 180 min. The circles mark the grains with a substantially higher Zn signal.

a PANalytical X′Pert Pro MRD diffractometer with Cu Kα radiation (1.54 Å). The TEM analysis of nanobelts was carried out with a JEOL 2010 TEM operated at 200 kV. The surface composition of the ZnO nanostructures was analyzed by X-ray photoelectron spectroscopy (XPS) using a Thermo-VG Scientific ESCALab 250 Microprobe with a monochromatic Al Kα source (1486.6 eV), capable of an energy resolution of 0.4–0.5 eV full width at half-maximum.

2.3. Glucose Oxidase Assay and SDS–PAGE Analysis of Proteins in Nanobelt-Like Structures. The activities of GOx surface-immobilized on ZnO NBS and embedded GOx-ZnO NBS were assayed using UV–vis spectroscopy at 510 nm and 25 °C. GOx catalyzes the oxidation of β-D-glucose to D-glucono-δ-lactone with the concurrent release of hydrogen peroxide. The reaction velocity can be determined by an increase in absorbance at 510 nm resulting from the oxidation of *p*-hydroxybenzoic acid and 4-aminoantipyrine through a peroxidase coupled system. Accordingly, three assay solutions were prepared, i.e.: Solution 1, 10 mM *p*-hydroxybenzoic acid in 60 mM potassium phosphate buffer (pH 7.0); Solution 2, 500 mM D-glucose in Milli-Q water; and Solution 3, 1.5 mg of GOx in 100 mM potassium phosphate buffer (pH 7.0), which was used for the measurement of standard enzyme activity. Solution 1 (2 mL) was pipetted into a cuvette containing the substrate deposited with ZnO NBS, with a small magnetic bar placed at the bottom of the cuvette for gently stirring, followed by 0.5 mL of Solution 2. The absorbance increments at 510 nm were recorded for 10 min after the mixture was incubated in the spectrophotometer for 1 min to achieve temperature equilibration. SDS–PAGE analysis of proteins on or inside the ZnO NBS samples was carried out using Phast gradient gel (10–15%, GE healthcare, QC). The "surface GOx" content was measured by washing both the surface-immobilized and embedded GOx-ZnO NBS samples in a 6 M urea solution. To measure the "bulk GOx", both samples were dissolved in 0.5 mL HCl solutions (50 mM) for 30 s. All protein fractions were precipitated with 10% trichloroacetic acid and cleaned up with acetone and then dried with Vac-spin centrifugation. The resulting dried powder was solubilized in 10 μL of the SDS–PAGE sample loading buffer.

3. RESULTS AND DISCUSSION

3.1. ZnO Nanobelt-Like Structures: Morphology and Growth Mechanism. Figure 1 shows the SEM images of NBS at different magnifications grown on a PET substrate in an electrolyte solution of 0.1 M $Zn(NO_3)_2 \cdot 6H_2O$ mixed with 0.1 M KCl (serving as the supporting electrolyte) at 0 °C for 180 min. These NBS are found to grow uniformly over the entire

substrate (10 mm × 5 mm), as shown in Figure 1a. The NBS also appear to be slender and flexible, with the longer belts bending over and lying nearly horizontal on the substrate surface (Figure 1d–f). The length, width, and thickness of these NBS are measured to be in the ranges of 5–10 μm, 50–400 nm, and 20–100 nm, respectively (Figure 1). Unlike the nanobelts previously reported to have a uniform thickness across the width,[21,29,31] the NBS obtained in the present work have an oval-shaped cross section, with the central part thicker than the edge (Figure 1c, inset). Closer examination of the relatively rough textures of the NBS reveals thin ribbons or threadlike structures merging into one another (Figure 1f). To further characterize the composition of the NBS samples, EDX elemental mapping of zinc and oxygen has been performed for a selected region of less densely populated NBS shown in Figure 2a. As expected, strong intensities are detected within the NBS locations in the Zn (Figure 2b) and O elemental maps (Figure 2c). However, some of the grains/particles in Figure 2a appear to exhibit mainly the Zn signal, with substantially less O signal. This indicates that the grains deposited over the substrate are primarily zinc, whereas the NBS are ZnO. The formation of metallic zinc is attributed to the low deposition temperature and a high negative applied potential used for the electrodeposition. Similar ZnO NBS have also been deposited on ITO-glass, suggesting that the substrate does not play an important role in their formation.

To gain a more detailed understanding of the growth evolution and formation mechanism of ZnO NBS, we repeated the electrodeposition by systematically varying the deposition time while keeping all other parameters constant. Figure 3 shows the growth evolution of NBS on a PET substrate at different deposition times. After 1 min of deposition, discontinuous growth of gel-like ZnO nanostructures is observed (Figures 3a and 3b). These structures became a continuous film after 5 min of deposition (SEM images not shown). After 10 (Figure 3c) and 15 min (Figure 3d) of deposition, whisker structures appeared to emerge from the grainlike structures. Direct growth of NBS on the PET substrate has also been found in localized areas as shown in Figure 3d. Figure 3e shows the corresponding EDX spectra of two different regions marked in Figure 3d, which show a higher stoichiometric ratio of Zn:O in the grain regions as compared to the NBS regions, indicating the codeposition of Zn grains during electrodeposition. This is in accord with our EDX mapping result shown in Figure 2, which also reveals the presence of Zn grains. With increasing the deposition time to 30 (Figure 3f), 60, and 120 min (Figures 3g and 3h), the lengths and integrity of the NBS became more developed, while their uniformity over the substrate continued to improve. Figure 4 shows a schematic

18151

dx.doi.org/10.1021/jp205747z |*J. Phys. Chem. C* 2011, 115, 18149–18156
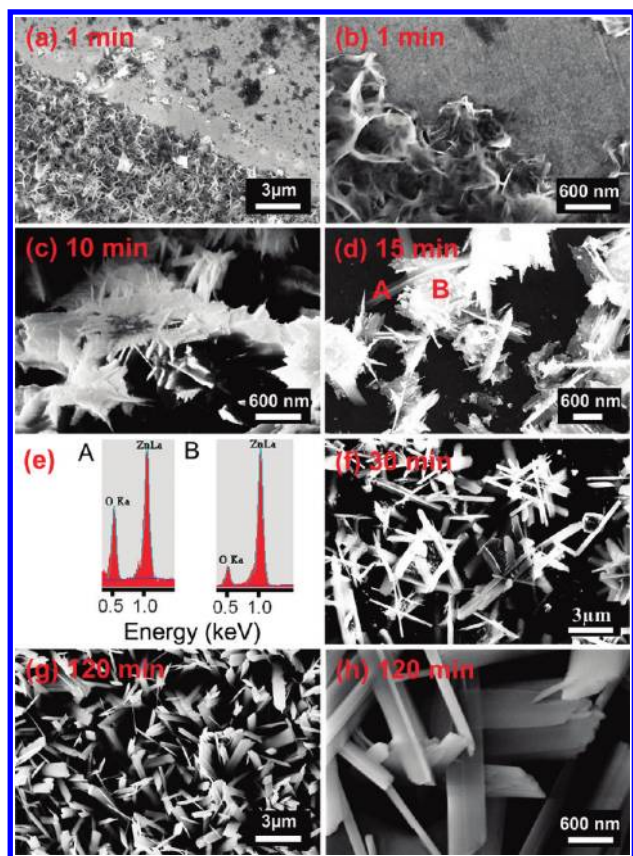
Figure 3. SEM images of ZnO nanobelt-like structures electrodeposited at 0 °C on conducting PET substrates for a total deposition time of (a,b) 1, (c) 10, (d) 15, (f) 30, and (g,h) 120 min and (e) EDX spectra of regions A and B marked in (d).
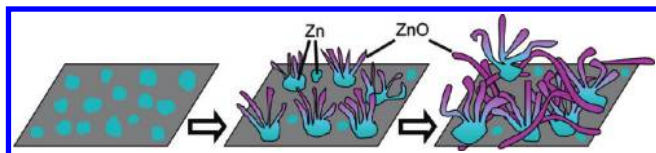

Figure 4. Schematic growth model of ZnO nanobelt-like structures at 0 °C.

diagram of growth evolution of NBS on a conducting PET substrate at 0 °C.

In accord with the earlier studies,[6,45−47] a plausible mechanism for the formation of ZnO NBS can be envisioned as below. The $Zn(NO_3)_2 \cdot 6H_2O$ salt used as the electrolyte produces Zn^{2+} ions and NO_3^- in the aqueous solution. The detailed reaction mechanism occurring during the electrodeposition of ZnO is discussed elsewhere.[45,48] Briefly, reduction of nitrate to nitrite ions generates hydroxide ions at the cathode surface.

$$NO_3^- + H_2O + 2e^- \rightarrow NO_2^- + 2OH^- \tag{1}$$

The Zn^{2+} ions undergo a hydroxylation reaction with the OH^- ions in the solution to produce $Zn(OH)_2$ on the cathode surface, which is then converted to ZnO upon dehydration.

$$Zn^{2+} + 2OH^- \rightarrow Zn(OH)_2 \tag{2}$$

$$Zn(OH)_2 \rightarrow ZnO + H_2O \tag{3}$$
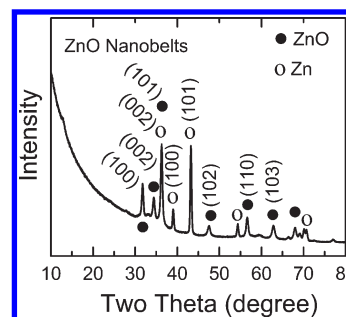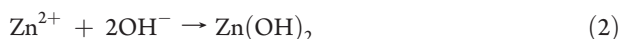
Figure 5. GIXRD pattern of the ZnO nanobelt-like structures electrodeposited on an ITO-glass substrate at 0 °C. The crystallographic planes for the prominent ZnO and Zn features are identified.

The overall reaction can therefore be written as

$$Zn^{2+} + NO_3^- + 2e^- \rightarrow ZnO + NO_2^- \tag{4}$$

In addition to the above reactions, the Zn^{2+} ions can also be directly reduced to Zn. In the present work, we observed the presence of both Zn and ZnO, indicating the contributions from both reactions during the growth evolution. Our finding shows that the morphology is related to the composition of the nanostructures deposited at 0 °C, with the individual NBS and grainlike structures consisting of ZnO and Zn, respectively. It should be noted that no Zn was found in the earlier study even though the deposition was carried out in the same electrolyte with the same concentration [0.1 M $Zn(NO_3)_2 \cdot 6H_2O$] at the same applied potential (−1.4 V),[49] which could be due to the higher temperature (70 °C) used in the electrodeposition, unlike the present work. The morphology of the agglomerated flower-type ZnO nanostructures in the earlier study[49] is also strikingly different from that in the present work. While the exact mechanism is not clear, the use of a low deposition temperature (0 °C), a large negative applied potential (−1.4 V), and a high electrolyte concentration (0.1 M) appears to be the key to attaining an intricate balance of the kinetic reaction rates between the hydroxylation and dehydration reactions to facilitate the evolution of the quasi-1D beltlike nanostructure. The deposition temperature and electrolyte concentration have significant effects on the formation of ZnO nanostructures. We reported the evolution of 2D ZnO nanowalls from nanosheets by increasing the deposition temperature from room temperature to 70 °C at −1.1 V.[50] The effect of electrolyte concentration on the formation of diverse ZnO nanostructures such as nanowalls, nanodisks, nanospikes, nanopillars, and nanospheres has been discussed elsewhere.[45,51] From our previous studies, it can be concluded that the deposition temperature has a milder effect than the electrolyte concentration. Two-dimensional nanostructures with different morphologies such as nanowalls, nanosheets, and NBS are obtained from an electrolyte solution of 0.1 M $Zn(NO_3)_2 \cdot 6H_2O$ mixed with 0.1 M KCl at a temperature of 70, 22, and 0 °C, respectively. It should be noted that the applied potential has been increased to −1.4 V to obtain NBS because no NBS is obtained at −1.1 V. Furthermore, the involvement of Cl^- ions in the NBS formation supports the conventional 2D ZnO growth mechanism in the electrodeposition process.[45,47] Although KCl is used as the supporting electrolyte (to increase the conductivity of the solution) for effective electrodeposition, our earlier work has shown that Cl^- ions are adsorbed on the (002) polar plane of ZnO, thereby restricting growth in that
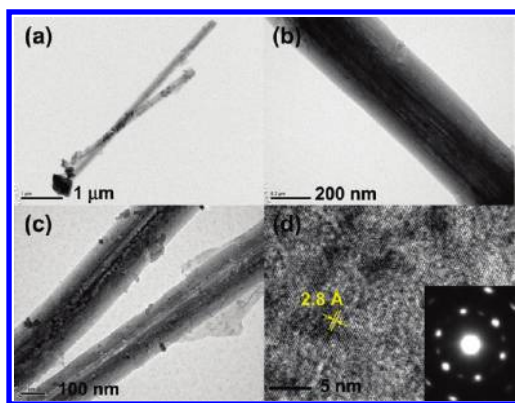
Figure 6. (a, b, and c) TEM images of typical nanobelt-like structures and (d) HRTEM image and diffraction pattern (inset) of a section of the nanostructure.

Figure 7. XPS survey spectrum for the nanobelt-like structures electro-deposited on an ITO-glass substrate at 0 °C.

direction.[45] An initial KCl concentration above 0.01 M is sufficient to induce lateral growth to produce 2D nanostructures (and in the present case quasi 1D structure because of reduced growth in the lateral direction), while below 0.01 M 1D ZnO nanostructural growth occurs.[52] The growth on the (002) plane, i.e., along the c-axis, which is also known as the fastest growth plane, normally produces 1D nanowires.[53] The obstruction of growth on the (002) plane of ZnO due to Cl⁻ adsorption redirects the growth on the side facets producing 2D nanostructures such as nanowalls,[45] platelet-like crystals,[47] and NBS in the present work.

3.2. Structural Properties and Composition of ZnO Nanobelt-Like Structures. Figure 5 shows the glancing-incidence X-ray diffraction (GIXRD) spectrum of NBS grown on an ITO-glass substrate at 0 °C. The sharp diffraction peaks confirm the crystalline nature of the electrodeposited nanomaterials. All the major diffraction peaks are matched to the wurtzite ZnO structure (JCPDS 01-070-2551), except for two features at 36.2° and 43.2°, which can be assigned to, respectively, the Zn(002) [also coinciding with ZnO(101)] and Zn(101) planes (JCPDS 01-087-0713). The observation of Zn diffraction features is due to the underlying grainlike layer grown on the substrate prior to NBS nucleation, as observed in the EDX mapping (Figure 2). It is of interest to note that there is no peak attributable to the chlorinated zinc hydroxyl salt, i.e., Zn_5-$(OH)_8Cl_2 \cdot H_2O$ (Simonkolleite), normally found for 2D ZnO nanowalls or nanoplates obtained from the same electrolyte concentration but at a higher temperature (70 °C) and a less negative deposition potential (−1.1 V).[45,54] This suggests that the use of a low deposition temperature and a large negative potential in the present work suppresses the formation of the chlorinated zinc hydroxyl salt and promotes the reduction of Zn^{2+} to metallic zinc.

Transmission electron microscopy (TEM) was employed to further characterize the microstructures of individual ZnO NBS grown at 0 °C. The typical TEM images obtained from the NBS shown in Figure 6 support the morphologies illustrated in the SEM images (Figure 1). In particular, the contrast variations of the TEM images in Figure 6b and 6c clearly reflect the nonuniform thickness of NBS across the width, with a thicker central region than the thinner edges. Figure 6d shows a corresponding high-resolution TEM image of a NBS (Figure 6c), with the 2D lattice fringes and the corresponding spots observed in the electron diffraction pattern (inset) both affirming the single-crystalline
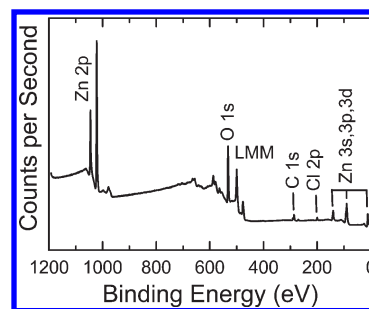
nature of the NBS. The interlayer spacing between the fringes is measured to be 2.8 Å corresponding to the $(10\bar{1}0)$ [or (100)] crystal plane of ZnO. The diffraction pattern of the corresponding high-resolution TEM image can be indexed as hexagonal ZnO along the [0001] (or [002]) axis, indicating the growth of the NBS occurring in the $(10\bar{1}0)$ direction. Both of our XRD and TEM results show that the as-synthesized nanomaterials have a crystal structure similar to that of ZnO nanobelts, nanodisks, and nanowalls.[11,31,33,52,55] Therefore, even though these NBS have a thicker central region and grow as 1D structures the obvious side facet growth makes them pseudo 1D nanostructures.

A detailed depth-profiling X-ray photoelectron spectroscopy (XPS) study has been performed to characterize the chemical-state composition of the as-synthesized NBS. Figure 7 shows a typical XPS survey spectrum of the ZnO NBS sample. In particular, the survey spectrum shows the presence of weak Cl 2p features, in addition to the prominent Zn 2p and O 1s features. A minor C 1s feature due to the surface contaminants arising from sample handling is also observed. Figure 8 shows the XPS spectra of the Zn 2p, O 1s, and Cl 2p regions as a function of sputtering time. For the as-deposited sample (at 0 s sputtering time), the XPS peaks are found to be located at much higher BEs than their respective reference positions,[56] which can be attributed to minor sample charging due to the presence of a residual amount of the nonconducting $Zn(OH)_2$ at the surface. Upon sputtering for 180 s, the spectral envelopes of Zn 2p, O 1s, and Cl 2p are found to shift toward the lower BE side and settle at the respective reference positions due to removal of the nonconducting $Zn(OH)_2$ at the surface. In the formation mechanism of 2D ZnO nanostructures such as nanoplates and nanowalls,[45−47] the role of the Cl⁻ ions as the capping agent is well-known and has been described above. In this mechanism, the electronegative Cl⁻ ions adsorb onto the polar (+0001) plane of ZnO and hinder growth in the [0001] direction (the c-axis), thereby promoting the growth in the other directions, i.e., $[10\bar{1}0]$, to form the 2D ZnO nanostructures. The presence of Cl $2p_{3/2}$ ($2p_{1/2}$) at 198.8 eV (200.4 eV) in the XPS spectra after 180 s of sputtering (Figure 8c) suggests that the quasi 1D growth of ZnO NBS follows a similar capping mechanism. The corresponding O 1s spectrum of ZnO NBS after 180 s of sputtering (Figure 8b) reveals two components at 531.8 and 530.3 eV corresponding to $Zn(OH)_2$ and ZnO, respectively, in good agreement with the literature values.[57,58] The $Zn(OH)_2$ component is found to weaken, while the ZnO component strengthens with increasing sputtering time, which indicates that $Zn(OH)_2$ is present only in the near-surface region. Figure 8a shows the corresponding Zn $2p_{3/2}$ ($2p_{1/2}$) feature at 1021.7 (1044.8) eV, with the observed spin−orbit splitting of 23.0 eV (±0.1 eV) in excellent accord
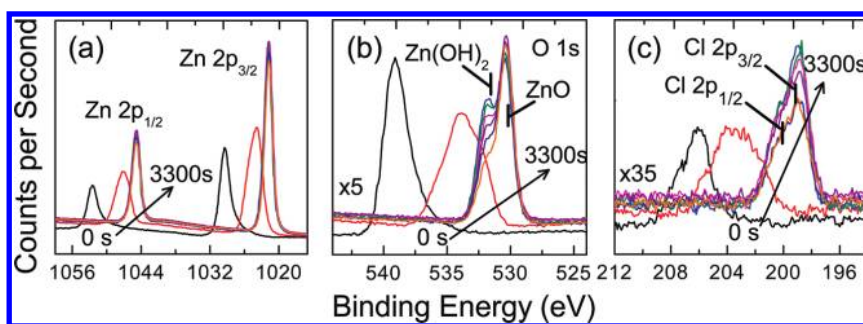
Figure 8. XPS spectra of (a) Zn 2p, (b) O 1s, and (c) Cl 2p regions as a function of sputtering time from 0 s, 60 s, 180 s, 300 s, 600 s, 1200 s, 2100 s, to 3300 s for the nanobelt-like structures electrodeposited on an ITO-glass substrate at 0 °C.
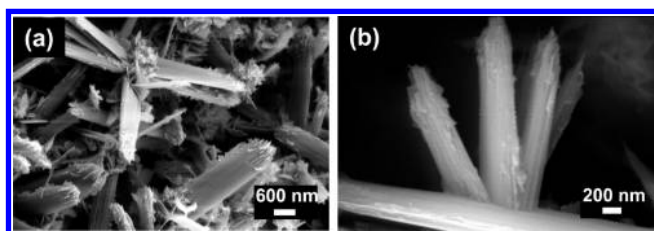
Figure 9. SEM images of embedded GOx-ZnO nanobelt-like structures, electrodeposited on an ITO-glass substrate at 0 °C from 10 mL electrolyte of 0.1 M $Zn(NO_3)_2 \cdot 6H_2O$ mixed with 0.1 M KCl and 5 mg of GOx for 1 h.

with the literature value of 22.97 eV.[56] The single-peak nature of the Zn $2p_{3/2}$ ($2p_{1/2}$) feature indicates the presence of only the divalent Zn(II) oxidation state, corresponding to both $Zn(OH)_2$ and ZnO. The absence of a metallic Zn peak suggests that the Zn grainlike layer is well underneath the NBS film, considerably beyond the sputtering depth range used in the present XPS analysis.

3.3. GOx-Embedded ZnO Nanobelt-Like Structures and Their Properties. The present low-temperature deposition method enables us to directly integrate a biomolecule into the ZnO NBS during growth. Here, we demonstrate this important advantage of the new method in producing a bioactive nanocomposite using GOx as our test biomolecule. Due to the large difference in the isoelectronic point between GOx and ZnO, GOx is easily immobilized on the ZnO surface by a simple dipping method.[59] To incorporate GOx into the ZnO NBS in the present work, electrodeposition was performed in a zinc nitrate electrolyte mixed with GOx, with all other deposition parameters fixed. During deposition, the negatively charged GOx molecules were readily bound to the positively charged (0001) plane of ZnO and were embedded into the NBS. Figures 9a and 9b show the SEM images of the embedded GOx-ZnO NBS deposited on ITO-glass for 1 h. The embedded GOx-ZnO NBS were found to have morphology rather similar to that of ZnO NBS but with slightly higher surface roughness and distortions as appeared in the SEM images (Figure 9). This is believed to be due to the involvement of GOx during the growth of ZnO NBS. To measure the GOx activity and ascertain the incorporation of GOx into the NBS, enzymatic activity and sodium dodecyl sulfate polyacrylamide gel electrophoresis (SDS−PAGE) analysis of protein contents in embedded GOx-ZnO NBS were performed. The results are compared with that obtained for GOx surface-immobilized on ZnO NBS after growth. Parts (a), (b), and (c) of Figure 10 show the schematic models of pristine ZnO NBS and
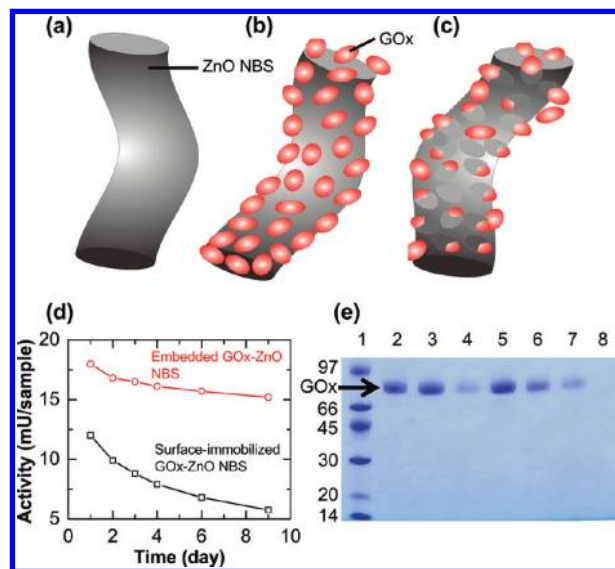
Figure 10. Schematic model diagram of ZnO nanobelt-like structures (a) as-synthesized without GOx and (b) with GOx surface-immobilized after growth and (c) with GOx directly embedded during growth. (d) Operational stability of embedded and surface-immobilized GOx-ZnO nanostructures as a function of storage time at 4 °C. (e) SDS−PAGE analysis of embedded and surface-immobilized GOx-ZnO nanostructures after 9 days. Lane 1, molecular weight marker in kilodalton (kDa); Lane 2, GOx standard; Lanes 3, 4, and 5, the "total GOx", "surface GOx", and "bulk GOx", respectively, of embedded GOx-ZnO nanostructures; Lanes 6, 7, and 8, the "total GOx", "surface GOx", and "bulk GOx", respectively, of the surface-immobilized GOx-ZnO nanostructures.

surface-immobilized and embedded GOx-ZnO NBS, respectively. In Figure 10d, we compare the GOx activities of the surface-immobilized and embedded GOx-ZnO NBS. Evidently, the GOx activity of the embedded GOx-ZnO NBS not only is considerably higher (by at least 50% initially) but also remains more stable with less degradation over an extended period of time compared to that of the surface-immobilized GOx-ZnO NBS. In the embedded GOx-ZnO NBS, a remarkably smaller reduction in the GOx activity (of less than 15%) was observed over the 9-day test period (Figure 10d), compared to that of the surface-immobilized GOx-ZnO NBS. Although the latter still maintained a strong enzymatic activity based on the assay of enzyme activity, it has lost over 53% of its initial activity in 9 days. This suggests that in the case of embedded GOx-ZnO NBS GOx was incorporated deep into the structures of the NBS and

therefore not easily washed out by repeated measurements. However, in the case of the surface-immobilized sample, GOx was slowly removed during washing after each measurement. Furthermore, at the end of the 9-day stability test period, the protein contents in the embedded and surface-immobilized GOx-ZnO NBS were analyzed by SDS—PAGE (Figure 10e). As observed from the intensity (Figure 10e), a higher quantity of "total GOx" (corresponding to the total amount of GOx) is observed in the embedded GOx-ZnO NBS (lane 3) as compared to surface-immobilized GOx-ZnO NBS (lane 6). The "surface GOx" was measured by washing both samples in a strong 6 M urea solution. As expected, the intensity of GOx for the surface-immobilized NBS (lane 7) is slightly higher than that of the embedded GOx-ZnO NBS (lane 4). These samples were then dissolved in HCl to measure the "bulk GOx", i.e., GOx embedded inside the respective NBS. Almost negligible "bulk GOx" intensity is observed from the surface-immobilized NBS (lane 8) relative to embedded GOx-ZnO NBS (lane 5), which confirms the direct incorporation of GOx into the structures of NBS during the deposition. It should be noted that the GOx loading time (equivalent to the deposition time) for embedded GOx-ZnO NBS was considerably shorter (1 h) than that of surface-immobilized GOx-ZnO NBS (24 h of dipping). The higher activity, longer stability, and shorter enzyme loading time for the embedded GOx-ZnO NBS therefore all illustrate a highly efficient process of producing bioactive nanomaterials when compared to the surface-immobilized methods.

4. CONCLUSIONS

In summary, quasi one-dimensional ZnO NBS have been grown on both conducting PET and ITO-glass substrates using a simple, one-step, template-free electrochemical technique for the first time at 0 °C. Our microscopic studies on the as-synthesized NBS show a unique oval-shape cross-sectional morphology. The high-resolution TEM and electron diffraction pattern confirm the single-crystalline structure of individual NBS with a growth direction of $[10\bar{1}0]$. We believe that the low electrodeposition temperature and higher negative applied potential offer an optimal set of kinetic conditions for the competing reaction steps (hydroxylation, dehydration, and Cl^- capping) in the production of the ZnO NBS. Furthermore, we have successfully demonstrated the direct incorporation of GOx into the structure of the ZnO NBS during growth, and these embedded GOx-ZnO NBS are found to be more active and stable when compared to the surface-immobilized GOx-ZnO NBS. The present direct incorporation approach of using low-temperature growth of nanobelts at 0 °C can be extended to other biomolecules, for developing novel bionanocomposites. As illustrated in the present work, the substantial increase in the retention time of biomolecules inside these bionanocomposites could lead to significant improvement in slow-release drug delivery and extended-use biosensor applications.

■ AUTHOR INFORMATION

Corresponding Author
*E-mail: tong@uwaterloo.ca.

Present Address
[†]Materials Science Centre, Indian Institute of Technology, Kharagpur, India 721 302.

■ ACKNOWLEDGMENT

■ REFERENCES

(1) Gao, P. X.; Lao, C. S.; Ding, Y.; Wang, Z. L. Metal/semiconductor Core/shell Nanodisks and Nanotubes. *Adv. Funct. Mater.* **2006**, *16*, 53–62 and references therein.

(2) Ng, H. T.; Li, J.; Smith, M. K.; Nguyen, P.; Cassell, A.; Han, J.; Meyyappan, M. Growth of Epitaxial Nanowires at the Junctions of Nanowalls. *Science* **2003**, *300*, 1249.

(3) Huang, M. H.; Mao, S.; Feick, H.; Yan, H.; Wu, Y.; Kind, H.; Weber, E.; Russo, R.; Yang, P. Room-Temperature Ultraviolet Nanowire Nanolasers. *Science* **2001**, *292*, 1897–1899.

(4) Vayssieres, L. Growth of Arrayed Nanorods and Nanowires of ZnO from Aqueous Solutions. *Adv. Mater.* **2003**, *15*, 464–466.

(5) Tian, Z. R.; Voigt, J. A.; Liu, J.; Mckenzie, B.; Mcdermott, M. J.; Rodriguez, M. A.; Konishi, H.; Xu, H. Complex and Oriented ZnO Nanostructures. *Nat. Mater.* **2003**, *2*, 821–826.

(6) Peulon, S.; Lincot, D. Cathodic Electrodeposition from Aqueous Solution of Dense or Open-structured Zinc Oxide Films. *Adv. Mater.* **1996**, *8*, 166–170.

(7) Liu, R.; Vertegel, A. A.; Bohannan, E. W.; Sorenson, T. A.; Switzer, J. A. Epitaxial Electrodeposition of Zinc Oxide Nanopillars on Single-Crystal Gold. *Chem. Mater.* **2001**, *13*, 508–512.

(8) Xu, S.; Wei, Y.; Kirkham, M.; Liu, J.; Mai, W.; Davidovic, D.; Snyder, R. L.; Wang, Z. L. Patterned Growth of Vertically Aligned ZnO Nanowire Arrays on Inorganic Substrates at Low Temperature without Catalyst. *J. Am. Chem. Soc.* **2008**, *130*, 14958–14959.

(9) Li, J.; Srinivasan, S.; He, G. N.; Kang, J. Y.; Wu, S. T.; Ponce, F. A. Synthesis and Luminescence Properties of ZnO Nanostructures Produced by the Sol—gel Method. *J. Cryst. Growth* **2008**, *310*, 599–603.

(10) Wu, G. S.; Xie, T.; Yuan, X. Y.; Li, Y.; Yang, L.; Xiao, Y. H.; Zhang, L. D. Controlled Synthesis of ZnO Nanowires or Nanotubes via Sol—gel Template Process. *Solid State Commun.* **2005**, *134*, 485–489.

(11) Cao, B.; Cai, W.; Li, Y.; Sun, F.; Zhang, L. Ultraviolet-light-emitting ZnO Nanosheets Prepared by a Chemical Bath Deposition Method. *Nanotechnology* **2005**, *16*, 1734.

(12) Cao, B.; Cai, W. From ZnO Nanorods to Nanoplates: Chemical Bath Deposition Growth and Surface-Related Emissions. *J. Phys. Chem. C* **2008**, *112*, 680–685.

(13) Ku, C. -H.; Wu, J. -J. Chemical Bath Deposition of ZnO Nanowire—nanoparticle Composite Electrodes for Use in Dye-sensitized Solar Cells. *Nanotechnology* **2007**, *18*, 505706.

(14) Pradhan, D.; Kumar, M.; Ando, Y.; Leung, K. T. Efficient Field Emission from Vertically Grown Planar ZnO Nanowalls on an ITO—glass Substrate. *Nanotechnology* **2008**, *19*, 035603.

(15) Gao, P. X.; Song, J.; Liu, J.; Wang, Z. L. Nanowire Piezoelectric Nanogenerators on Plastic Substrates as Flexible Power Sources for Nanodevices. *Adv. Mater.* **2007**, *19*, 67–72.

(16) Greene, L. E.; Law, M.; Goldberger, J.; Kim, F.; Johnson, J. C.; Zhang, Y.; Saykally, R. J.; Yang, P. Low-Temperature Wafer-Scale Production of ZnO Nanowire Arrays. *Angew. Chem., Int. Ed.* **2003**, *42*, 3031–3034.

(17) Yang, H. Y.; Lau, S. P.; Yu, S. F.; Huang, L.; Tanemura, M.; Tanaka, J.; Okita, T.; Hng, H. H. Field Emission from Zinc Oxide Nanoneedles on Plastic Substrate. *Nanotechnology* **2005**, *16*, 1300.

(18) Rica, de la R.; Matsui, H. Urease as a Nanoreactor for Growing Crystalline ZnO Nanoshells at Room Temperature. *Angew. Chem., Int. Ed.* **2008**, *47*, 5415–5417.

(19) Jung, S. -H.; Oh, E.; Lee, K. -H.; Yang, Y.; Park, C. G.; Park, W.; Jeong, S. -H. Sonochemical Preparation of Shape-Selective ZnO Nanostructures. *Cryst. Growth Des.* **2008**, *8*, 265–269.

(20) Sun, H.; Luo, M.; Weng, W.; Cheng, K.; Du, P.; Shen, G.; Han, G. Room-temperature Preparation of ZnO Nanosheets Grown on Si

Substrates by a Seed-layer Assisted Solution Route. *Nanotechnology* **2008**, *19*, 125603.

(21) Yang, J.; Liu, G.; Lu, J.; Qiu, Y.; Yang, S. Electrochemical Route to the Synthesis of Ultrathin ZnO Nanorod/nanobelt Arrays on Zinc Substrate. *Appl. Phys. Lett.* **2007**, *90*, 103109.

(22) Tian, M.; Wang, J.; Kumar, N.; Han, T.; Kobayashi, Y.; Liu, Y.; Mallouk, T. E.; Chan, M. H. W. Observation of Superconductivity in Granular Bi Nanowires Fabricated by Electrodeposition. *Nano Lett.* **2006**, *6*, 2773–2780.

(23) Cao, H. L.; Qian, X. F.; Gong, Q.; Du, W. M.; Ma, X. D.; Zhu, Z. K. Shape- and Size-controlled Synthesis of Nanometre ZnO from a Simple Solution Route at Room Temperature. *Nanotechnology* **2006**, *17*, 3632.

(24) Oliveira, A. P. A.; Hochepied, J. -F.; Grillon, F.; Berger, M. -H. Controlled Precipitation of Zinc Oxide Particles at Room Temperature. *Chem. Mater.* **2003**, *15*, 3202–3207.

(25) Tseng, R. J.; Tsai, C.; Ma, L.; Ouyung, J.; Ozkan, C. S.; Yang, Y. Digital Memory Device Based on Tobacco Mosaic Virus Conjugated with Nanoparticles. *Nature Nanotechnol.* **2006**, *1*, 72–77.

(26) Ueno, T.; Koshiyama, T.; Tsuruga, T.; Goto, T.; Kanamaru, S.; Arisaka, F.; Watanabe, Y. Bionanotube Tetrapod Assembly by In Situ Synthesis of a Gold Nanocluster with (Gp5−His6)3 from Bacteriophage T4. *Angew. Chem., Int. Ed.* **2006**, *45*, 4508–4512.

(27) Umetsu, M.; Mizuta, M.; Tsumoto, K.; Ohara, S.; Takami, S.; Watanabe, H.; Kumagai, I.; Adschiri, T. Bioassisted Room-Temperature Immobilization and Mineralization of Zinc Oxide—The Structural Ordering of ZnO Nanoparticles into a Flower-Type Morphology. *Adv. Mater.* **2005**, *17*, 2571–2575.

(28) Mao, C.; Solis, D. J.; Reiss, B. D.; Kottmann, S. T.; Sweeney, R. Y.; Hayhurst, A.; Georgiou, G.; Iverson, B.; Belcher, A. M. Virus-Based Toolkit for the Directed Synthesis of Magnetic and Semiconducting Nanowires. *Science* **2004**, *303*, 213–217.

(29) Pan, Z. W.; Dai, Z. R.; Wang, Z. L. Nanobelts of Semiconducting Oxides. *Science* **2001**, *291*, 1947–1949.

(30) Lao, C.; Li, Y.; Wong, C. P.; Wang, Z. L. Enhancing the Electrical and Optoelectronic Performance of Nanobelt Devices by Molecular Surface Functionalization. *Nano Lett.* **2007**, *7*, 1323–1328.

(31) Wang, W.; Zeng, B.; Yang, J.; Poudel, B.; Huang, J.; Naughton, M. J.; Ren, Z. Aligned Ultralong ZnO Nanobelts and Their Enhanced Field Emission. *Adv. Mater.* **2006**, *18*, 3275–3278.

(32) Cheng, Y.; Xiong, P.; Fields, L.; Zheng, J. P.; Yang, R. S.; Wang, Z. L. Intrinsic Characteristics of Semiconducting Oxide Nanobelt Field-effect Transistors. *Appl. Phys. Lett.* **2006**, *89*, 093114.

(33) Kong, X. Y.; Ding, Y.; Wang, Z. L. Metal−Semiconductor Zn−ZnO Core−Shell Nanobelts and Nanotubes. *J. Phys. Chem. B* **2004**, *108*, 570–574.

(34) Lu, C.; Qi, L.; Yang, J.; Tang, L.; Zhang, D.; Ma, J. Hydrothermal Growth of Large-scale Micropatterned Arrays of Ultralong ZnO Nanowires and Nanobelts on Zinc Substrate. *Chem. Commun.* **2006** 3551–3553.

(35) Flint, K. P. The Long-term Survival of Escherichia Coli in River Water. *J. Appl. Bacteriol.* **1987**, *63*, 261–270.

(36) Alaejos, M. S.; Montelongo, F. J. G. Application of Amperometric Biosensors to the Determination of Vitamins and α-Amino Acids. *Chem. Rev.* **2004**, *104*, 3239–3266.

(37) Das, M.; Mishra, D.; Dhak, P.; Gupta, S.; Maiti, T. K.; Basak, A.; Pramanik, P. Biofunctionalized, Phosphonate-Grafted, Ultrasmall Iron Oxide Nanoparticles for Combined Targeted Cancer Therapy and Multimodal Imaging. *Small* **2009**, *5*, 2883–2893.

(38) Yang, N.; Uetsuka, H.; Nebel, C. E. Biofunctionalization of Vertically Aligned Diamond Nanowires. *Adv. Funct. Mater.* **2009**, *19*, 887–893.

(39) Tahir, M. N.; Natalio, F.; Therese, H. A.; Yella, A.; Metz, N.; Shah, M. R.; Mugnaioli, E.; Berger, R.; Theato, P.; Schroder, H. -C.; Muller, W. E. G.; Tremel, W. Enzyme-Mediated Deposition of a TiO₂ Coating onto Biofunctionalized WS₂ Chalcogenide Nanotubes. *Adv. Funct. Mater.* **2009**, *19*, 285–291.

(40) Bao, S. -J.; Li, C. M.; Zang, J. -F.; Cui, X. -Q.; Qiao, Y.; Guo, J. New Nanostructured TiO₂ for Direct Electrochemistry and Glucose Sensor Applications. *Adv. Funct. Mater.* **2008**, *18*, 591–599.

(41) Nosworthy, N. J.; McKenzie, D. R.; Bilek, M. M. A New Surface for Immobilizing and Maintaining the Function of Enzymes in a Freeze-Dried State. *Biomacromolecules* **2009**, *10*, 2577–2583.

(42) Kim, S. E.; Choi, H. W.; Lee, H. J.; Chang, J. H.; Choi, J.; Kim, K. J.; Lim, H. J.; Jun, Y. J.; Lee, S. C. Designing a Highly Bioactive 3D Bone-regenerative Scaffold by Surface Immobilization of Nano-hydroxyapatite. *J. Mater. Chem.* **2008**, *18*, 4994–5001.

(43) Martinez, K.; Estevez, M. -C.; Wu, Y.; Phillips, J. A.; Medley, C. D.; Tan, W. Locked Nucleic Acid Based Beacons for Surface Interaction Studies and Biosensor Development. *Anal. Chem.* **2009**, *81*, 3448–3454.

(44) Riegler, J.; Ditengou, F.; Palme, K.; Nann., T. Blue Shift of CdSe/ZnS Nanocrystal-labels upon DNA-hybridization. *J. Nanobiotechnol.* **2008**, *6*, 7.

(45) Pradhan, D.; Leung, K. T. Controlled Growth of Two-Dimensional and One-Dimensional ZnO Nanostructures on Indium Tin Oxide Coated Glass by Direct Electrodeposition. *Langmuir* **2008**, *24*, 9707–9716.

(46) Tena-Zaera, R.; Elias, J.; Wang, G.; Levy-Clement, C. Role of Chloride Ions on Electrochemical Deposition of ZnO Nanowire Arrays from O₂ Reduction. *J. Phys. Chem. C* **2007**, *111*, 16706–16711.

(47) Xu, L.; Guo, Y.; Liao, Q.; Zhang, J.; Xu, D. Morphological Control of ZnO Nanostructures by Electrodeposition. *J. Phys. Chem. B* **2005**, *109*, 13519–13522.

(48) Yoshida, T; Komatsu, D.; Shimokawa, N.; Minoura, H. Mechanism of Cathodic Electrodeposition of Zinc Oxide Thin Films from Aqueous Zinc Nitrate Baths. *Thin Solid Films* **2004**, *451−452*, 166–169.

(49) Izaki, M.; Omi, T. Transparent Zinc Oxide Films Prepared by Electrochemical Reaction. *Appl. Phys. Lett.* **1996**, *68*, 2439–2440.

(50) Pradhan, D.; Leung, K. T. Vertical Growth of Two-Dimensional Zinc Oxide Nanostructures on ITO-Coated Glass: Effects of Deposition Temperature and Deposition Time. *J. Phys. Chem. C* **2008**, *112*, 1357–1364.

(51) Pradhan, D.; Leung, K. T. Template-free Single-step Electrochemical Synthesis of ZnO Hollow Nanospheres: Self-assembly of Hollow Nanospheres from Nanoparticles. *J. Mater. Chem. (Communication)* **2009**, *19*, 4092–4095.

(52) Pradhan, D.; Sindhwani, S.; Leung, K. T. Parametric Study on Dimensional Control of ZnO Nanowalls and Nanowires by Electrochemical Deposition. *Nanoscale Res. Lett.* **2010**, *5*, 1727–1736.

(53) Pauporte, T.; Cortes, R.; Froment, M.; Beaumont, B.; Lincot, D. Electrocrystallization of Epitaxial Zinc Oxide onto Gallium Nitride. *Chem. Mater.* **2002**, *14*, 4702–4708.

(54) Peulon, S.; Lincot, D. Mechanistic Study of Cathodic Electrodeposition of Zinc Oxide and Zinc Hydroxychloride Films from Oxygenated Aqueous Zinc Chloride Solutions. *J. Electrochem. Soc.* **1998** *145*, 864–874.

(55) Chen, Y. F.; Wang, R. M.; Zhang, H. Z.; Sun, X. C.; Zhang, Z. S.; Xing, Y. J.; Yu, D. P. TEM investigations on ZnO nanobelts synthesized via a vapor phase growth. *Micron* **2004**, *35*, 481–487.

(56) Moulder, J. F.; Stickle, W. F.; Sobol, P. E.; Bomben, K. D. *Handbook of X-ray Photoelectron Spectroscopy*; Chastain, J., Ed.; Perkin-Elmer Corporation: USA, 1992.

(57) Lu, Z. L.; Yan, G. Q.; Wang, S.; Zou, W. Q.; Mo, Z. R.; Lv, L. Y.; Zhang, F. M.; Du, Y. W.; Xu, M. X.; Xia, Z. H. Influence of the Oxidative Annealing Temperature on the Magnetism of (Mn, N)-codoped ZnO Thin Films. *J. Appl. Phys.* **2008**, *104*, 033919.

(58) Puchert, M. K.; Timbrell, P. Y.; Lamb, R. N. Postdeposition Annealing of Radio Frequency Magnetron Sputtered ZnO Films. *J. Vac. Sci. Technol. A* **1996**, *14*, 2220–2230.

(59) Wang, J. X.; Sun, X. W.; Wei, A.; Lei, Y.; Cai, X. P.; Li, C. M.; Dong, Z. L. Zinc oxide nanocomb biosensor for glucose detection. *Appl. Phys. Lett.* **2006**, *88*, 233106.

18156

dx.doi.org/10.1021/jp205747z |*J. Phys. Chem. C* 2011, 115, 18149–18156